



Available online at www.sciencedirect.com

ScienceDirect

Geochimica et Cosmochimica Acta

Geochimica et Cosmochimica Acta 309 (2021) 235–250

www.elsevier.com/locate/gca

Lack of redox cycling for nickel in the water column of the Eastern tropical north pacific oxygen deficient zone: Insight from dissolved and particulate nickel isotopes

Shun-Chung Yang ^{a,*}, Rachel L. Kelly ^a, Xiaopeng Bian ^a, Tim M. Conway ^b, Kuo-Fang Huang ^c, Tung-Yuan Ho ^d, Jacquelyn A. Neibauer ^e, Richard G. Keil ^e, James W. Moffett ^f, Seth G. John ^a

^a Department of Earth Sciences, University of Southern California, Los Angeles, CA, USA
 ^b College of Marine Science, University of South Florida, St Petersburg, FL, USA
 ^c Institute of Earth Sciences, Academia Sinica, Taipei, Taiwan
 ^d Research Center for Environmental Changes, Academia Sinica, Taipei, Taiwan
 ^e School of Oceanography, University of Washington, Seattle, WA, USA
 ^f Department of Biological Sciences, University of Southern California, Los Angeles, CA, USA

Received 3 April 2021; accepted in revised form 1 July 2021; Available online 3 July 2021

Abstract

Marine oxygen deficient zones (ODZs) promote unique plankton communities and redox environments which impact the cycling of biologically essential trace metals in the ocean. Here we use measurements of dissolved and particulate Ni concentrations and isotopes to investigate the biotic and abiotic processes controlling Ni cycling in the world's largest ODZ, located in the Eastern Tropical North Pacific (ETNP). We observed a negative correlation between dissolved Ni concentrations and isotopic composition (δ^{60} Ni) throughout the water column, such that Ni concentrations increased from roughly 3 nmol kg⁻¹ to 8 nmol kg⁻¹ over the upper 1000 m, while δ^{60} Ni values decreased by 0.2% from about +1.6% to +1.4%. These vertical patterns are characteristic of both the subtropical North and South Pacific, and can be explained by a combination of physical mixing of water masses and biological uptake and export, either with all of the Ni being bioavailable or with separate bioavailable and non-bioavailable Ni pools. Although evidence for additional Ni cycling processes such as sulfide precipitation or Ni sorption/desorption through Fe/Mn redox chemistry have been observed in other ODZs and euxinic waters, we found no clear evidence for these in either the redoxcline or low oxygen waters of the ETNP. Indeed, the relationship between dissolved [Ni] and δ^{60} Ni observed in the ETNP is similar to results reported elsewhere in the subtropical North and South Pacific, falling generally on a mixing line between a surface water endmember (dissolved [Ni] = 2 nmol kg⁻¹ and δ^{60} Ni = +1.7‰) and a deep-water endmember (dissolved [Ni] = 6-10 nmol kg⁻¹ and δ^{60} Ni = \sim +1.4%). While this surface water endmember is similar to that of the Atlantic, the deep endmember in the Pacific is approximately 0.1% heavier than deep Atlantic Ni. This subtle isotopic difference suggests gradual accumulation of isotopically heavy Ni isotopes in the deep ocean, consistent with recent evidence of heavy Ni remobilization during early diagenesis. Lastly, in the ETNP, particulate δ^{60} Ni is generally ~0.5\% lighter than the dissolved Ni pool, and this pattern is consistent across both the euphotic zone and redoxcline, suggesting that biological export from the euphotic zone is the primary source of particulate Ni to the deep ocean. © 2021 Elsevier Ltd. All rights reserved.

Keywords: Oxygen deficient zone; Eastern Tropical North Pacific; Nickel; δ⁶⁰Ni

^{*} Corresponding author.

E-mail address: shunchuy@usc.edu (S.-C. Yang).

1. INTRODUCTION

Nickel (Ni) has been of interest to marine chemists since the 1980s due to its ubiquitous nutrient-like distribution (Sclater et al., 1976; Bruland, 1980; Boyle et al., 1981). The relationship between the distribution of Ni and biological processes has been explored in several different studies, and Ni has been found to be biologically important through the identification of eight Ni-based enzyme systems, including urease, Ni-superoxide dismutase (Ni-SOD), and hydrogenases that are associated with nitrogen uptake and fixation (Ragsdale, 2009). Further, a Ni requirement has been identified in diverse marine phytoplankton including diatoms and picocyanobacteria (Price and Morel, 1991; Dupont et al., 2008), and the highest nickel requirements have been found in the diazotrophic cyanobacteria Trichodesmium, due to its elevated demand for Ni-SOD and uptake hydrogenases (Ho, 2013; Rodriguez and Ho, 2014). In addition to intracellular utilization, up to ~50% of the total Ni in diatoms has been attributed to incorporation in extracellular frustules (Twining et al., 2012).

Based on riverine input fluxes of Ni and the average oceanic Ni concentration, the turnover time of Ni in the ocean has been estimated at ~30 kyrs (Cameron and Vance, 2014), which is much longer than the ~1 kyr time-scale of ocean mixing. Consequently, deep waters dominate the supply of Ni to the surface ocean, and the coupled effects of deep-water mixing/advection and biological assimilation/export determine the distribution and cycling of Ni throughout the major ocean basins (Middag et al., 2020).

Marine oxygen deficient zones (ODZs; dissolved $O_2 \le 20 \text{ }\mu\text{mol kg}^{-1}$) host environments with unique redox reactions and microbial communities (Lam and Kuypers, 2011), both of which might influence the cycling of Ni in seawater. For instance, Ni has a great affinity for manganese-oxide surfaces (Peacock and Sherman, 2007), and the cycling of manganese (Mn) in ODZ chemoclines can affect vertical Ni distributions, as has been observed across the Black Sea redoxcline where the redox transformations of Mn oxide/Mn2+ are accompanied by significant Ni removal and desorption (Vance et al., 2016). The formation of metal sulfides in settling particles in ODZ water columns has also been proposed to be a potential sink for trace metals (Janssen et al., 2014). For example, such a process has been suggested to affect Cd in suboxic waters of the Eastern Tropical North and South Atlantic and the Northeast Pacific (Janssen et al., 2014; Conway and John, 2015; Guinoiseau et al., 2019), Zn in the Northeast Pacific ODZ (Janssen and Cullen, 2015), and, potentially, Ni in the deep sulfidic Black Sea (Vance et al., 2016). However, whether or not Ni sulfide forms in ODZ particles remains unknown. Finally, prokaryotic communities living in the Eastern Tropical South Pacific ODZ have been shown to exhibit enhanced uptake of Ni and other trace metals including Cd, Zn, Cu, Co and V (Ohnemus et al., 2017), which may be related to unique biochemical or enzymatic demands for trace metals by denitrifying and other nitrogen-cycling ODZ biota (Moffett et al., 2007; Glass et al., 2015).

Measurement of the isotopic composition of Ni (δ^{60} Ni) in marine samples can provide further insight into the biogeochemical cycling of Ni in the oceans; although the published dataset of δ^{60} Ni in the ocean lags the other bioactive metals in terms of data coverage (Conway et al., 2021), existing studies demonstrate that δ^{60} Ni is a powerful tool for studying Ni cycling processes that fractionate isotope ratios. A notable example is the small but substantial, and likely ubiquitous, preferential uptake of light Ni isotopes by phytoplankton (Δ^{60} Ni_{plankton-aqueous} $\approx -0.3\%$), which is reflected in oceanic dissolved δ^{60} Ni values: in much of the open ocean, dissolved δ^{60} Ni is heavier in the surface ocean than in the deep ocean and is anti-correlated with the log of Ni concentrations (Takano et al., 2017; Archer et al., 2020; Yang et al., 2020). Slightly larger biological fractionation effects ($\Delta^{60} Ni_{cell\text{-}aqueous} \approx -0.8\%$) are generated during Ni utilization by methanogens, which is believed to have been the prevailing process of methanogenesis on the early anoxic earth (Cameron et al., 2009). Even larger isotopic fractionations are generated by chemical processes such as when Ni is removed via abiotic Ni sorption onto Mn oxides $(\Delta^{60} \text{Ni}_{\text{particulate-aqueous}} \approx -4\%)$, as demonstrated in laboratory experiments (Sorensen et al., 2020) and across the Black Sea chemocline (Vance et al., 2016).

Previous demonstration that various Ni isotopic fractionations can be linked to specific biotic and abiotic processes motivates this study of the stable Ni isotopic composition of seawater and marine particles in the Eastern Tropical North Pacific (ETNP) ODZ, the world's largest marine ODZ. Seawater samples were collected for dissolved δ^{60} Ni analysis from three stations within the ODZ, and one station in an adjacent suboxic zone for comparison. At one of the ODZ stations, size-fractionated particles were also collected for elemental and isotopic composition analyses. Our Ni data are also compared to other environmental parameters such as dissolved oxygen, nutrients and water mass composition. Lastly, we compare the dissolved δ^{60} Ni and [Ni] from this study to previously published data and discuss the significant differences in δ⁶⁰Ni–[Ni] patterns between the Pacific and the Atlantic Oceans.

2. METHODS

2.1. Hydrographic background of study site

This study was carried out during two expeditions to the Eastern Tropical North Pacific off the coast of Mexico (Fig. 1). Stations P1 (20.4°N, 106.2°E) and P2 (17.0°N, 107.1°E) were first sampled aboard the R/V Sikuliaq in December 2017. In April 2018, while aboard the R/V Roger Revelle, stations P1 and P2 were sampled again, along with two new stations P3 (21.3°N, 105.7°E) and P4 (25.2°N, 112.71°E). Sampling stations P1, P2 and P3 are located in the tropical oxygen deficient zone (ODZ), where dissolved oxygen is quickly drawn down below 1 μ M in the top 50–100 m of the water column (Fig. 2). Station P4 is situated off the coast of Baja, California and is within a suboxic costal region where dissolved oxygen concentrations drop quickly below the euphotic zone but never below 2 μ M (Fig. 2).

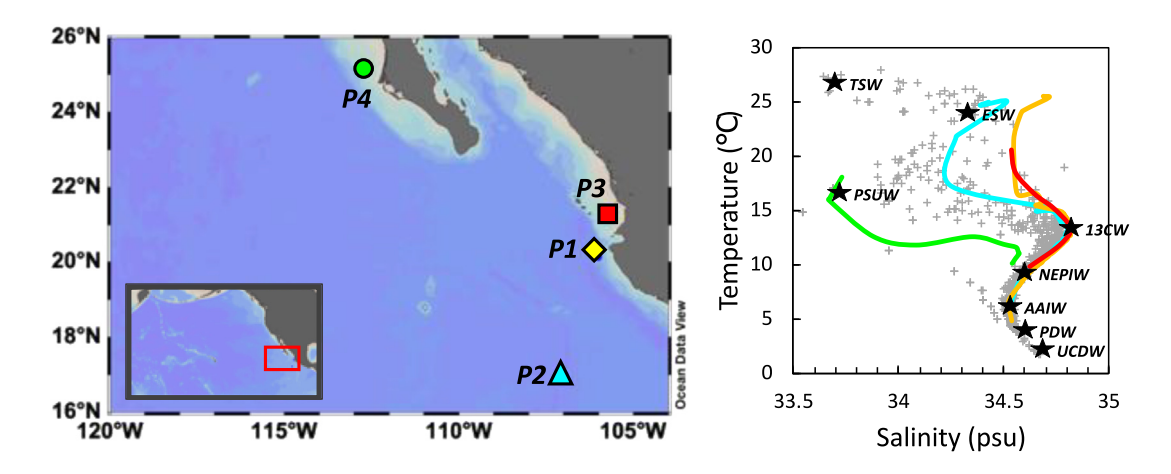


Fig. 1. Sampling sites and a T-S diagram of the study area. Stations P1, P2 and P3 are located in an oxygen deficient zone (ODZ) and P4 in a suboxic costal region. Gray crosses represent data from two previous cruises in 2018 showing the distribution of temperature and salinity in the area (Evans et al., 2020). Colored lines represent data from vertical profiles at sampling sites in this study including station P1 (yellow), P2 (blue), P3 (red) and P4 (green). Major water masses are labeled with stars and corresponding abbreviations including: Equatorial Surface Water (ESW), Pacific Subarctic Upper Water (PSUW), Antarctic Intermediate Water (AAIW), 13 °C Water (13CW), Northern Equatorial Pacific Intermediate Water (NEPIW), Pacific Deep Water (PDW), Upper Circumpolar Deep Water (UCDW) and Tropical Surface Water (TSW), all of which are defined in Fiedler and Talley (2006) and Evans et al. (2020). (For interpretation of the references to color in this figure legend, the reader is referred to the web version of this article.)

At the ODZ stations (P1, P2, and P3), the water columns are principally composed of three major water masses, Antarctic Intermediate Water (AAIW), Northern Equatorial Pacific Intermediate Water (NEPIW), and 13 °C Water (13CW). Salinity data shows a minimum value of 34.5 psu at the 600-700 m depth range (Fig. 1 and Supplementary Appendix A), which indicates the presence of AAIW. NEPIW, which is characterized by a temperature of ~9 °C and a salinity of ~34.6 psu (Fig. 1), slightly lower dissolved oxygen than AAIW and negligible nitrite production (Evans et al., 2020; Supplementary Appendix A) is located above AAIW, at ~400 m. NEPIW is formed by diapycnal mixing of Pacific Deep Water and AAIW, with some influence from North Pacific Intermediate Water (Bostock et al. 2010). Above NEPIW, centered at ~150 m is a water mass with a maximum salinity of 34.8 psu and temperature of 13 °C (Fig. 1, Supplementary Appendix A), which signifies the presence of 13CW. The most pronounced oxygen deficient conditions are found within 13CW, which is also characterized by extensive nitrate and iodate reductions (Evans et al., 2020; Moriyasu et al., 2020). 13CW originates in the Tasman Sea and is carried into the Eastern Pacific by the Equatorial Undercurrent (Fiedler & Talley, 2006; Evans et al., 2020). Above 13CW, the stations are composed of or influenced by Equatorial Surface Water (ESW) and other low salinity coastal waters (Fig. 1), which originate from a mixture of upwelled waters and the Equatorial Undercurrent (Fiedler and Talley, 2006).

At station P4, the water structure is less complex. NEPIW is present from ~150 to 550 m, accounting for most of our sampling depth range (Fig. 1; Supplementary Appendix A). Here, nitrite production within NEPIW is two orders of magnitude lower than at the ODZ stations.

At Station P4, low salinity Pacific Subarctic Upper Water (PSUW), which is formed in the subarctic and transported equatorward to the ETNP by the California Current (Evans et al., 2020), is located above NEPIW.

2.2. Reagents, standards, reference materials and samples

Seawater and suspended particle samples were collected from the upper 700 m of the water column using 5 L acid-cleaned Teflon-coated external-spring "Niskin-type" bottles (Ocean Test Equipment) on a powder-coated trace metal clean rosette (Sea-Bird Electronics). After collection, seawater was filtered through acid-washed 47 mm-diameter 0.2 μ m Supor polyethersulfone filters (Pall) and collected into acid-washed 1 L low density polyethylene bottles (Nalgene). The filters with suspended particles (>0.2 μ m) were then stored in acid-washed 50 mL polyethylene centrifuge tubes. On the 2017 cruise, 5 seawater samples from station P2 were collected by using an acid-washed 0.02 um hydrophobic filter (Acropak) to determine Ni concentrations and δ^{60} Ni within the 'soluble' phase (sometimes referred to as 'truly dissolved', <0.02 μ m).

Size-fractionated particles were also collected from the top 400 m of the water column at station P1 using a McLane pump (McLane Research Laboratories, Falmouth, MA, USA) equipped with a 4 mm mesh screen, a 142 mm-diameter Sefar polyester mesh prefilter (51 µm pore size) and a 142 mm-diameter 0.8 µm Pall Supor polyether-sulfone filter at each sampling depth. All filters and filter holders were acid leached before use based on the recommended methods in the GEOTRACES sample and sample-handling protocols (Cutter et al., 2017). Volumes filtered were between 100 and 800 L.

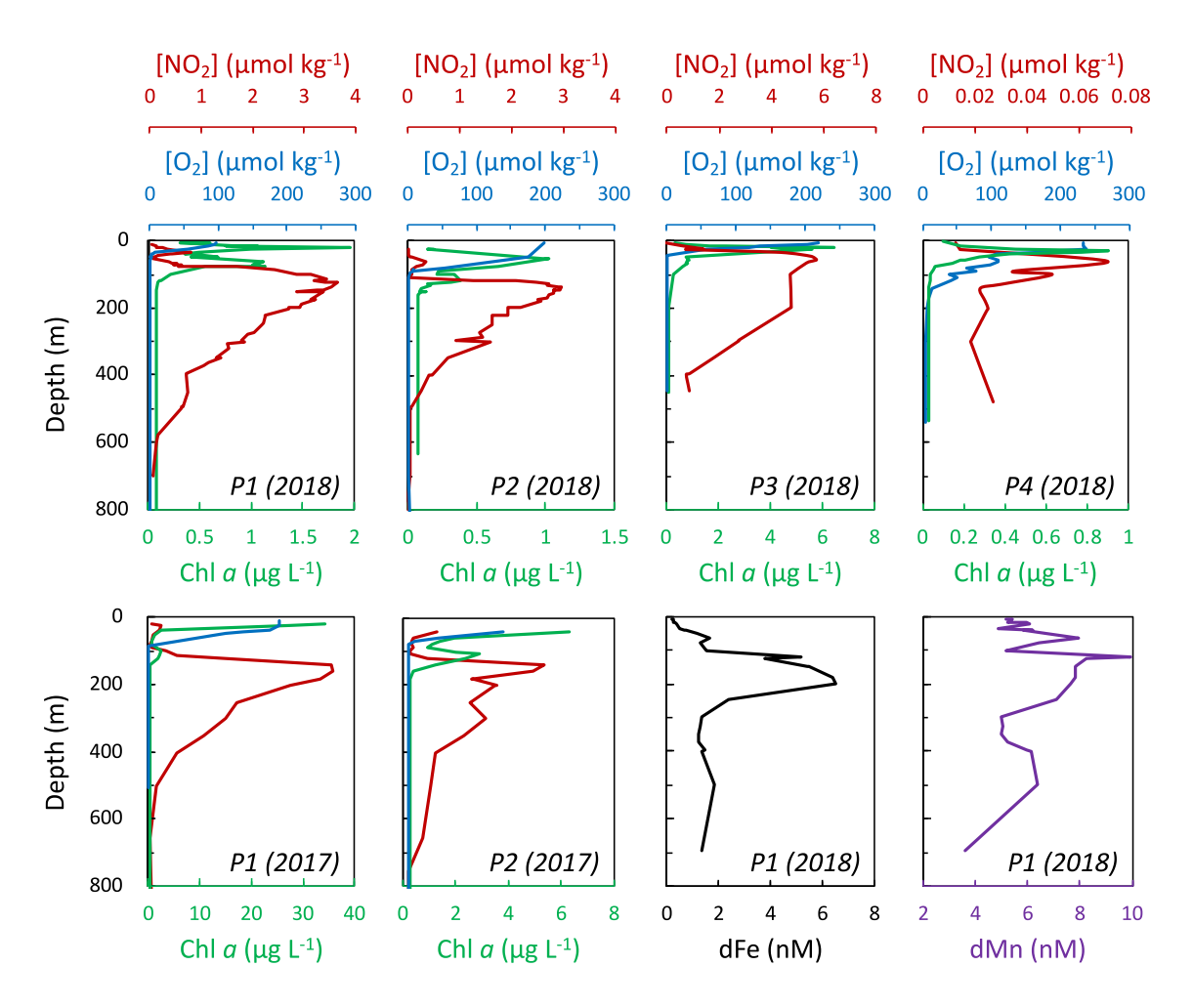


Fig. 2. Concentrations of nitrite (NO₂), dissolved oxygen (O₂), and chlorophyll a (Chl a) in the water columns of ODZ stations P1, P2, P3, and a suboxic station P4 collected during two separate cruises (2017 and 2018). NO₂, O₂, and Chl a values were extracted from a dataset published on the BCO-DMO data repository (Moffett, 2020). Dissolved Fe (dFe) and Mn (dMn) from the 2018 cruise are reported in this study.

All sample preparation was carried out in flow benches with Ultra Low Particulate Air (ULPA) filtration within a class 100 clean room at the University of Southern California. All reagents were purchased from the same manufacturer either as ultrapure reagents (BDH Aristar Ultra: HN₄OH and H₂O₂) or as lower grade reagents (BDH Aristar Plus: HCl, HNO₃, and acetic acid) which were then further purified by sub-boiling distillation in a PFA still (Savillex). Ultrapure water (Milli-Q; 18.2 M Ω) was used throughout. All steps involving concentrated acids were performed in acid-cleaned PFA teflon vials (Savillex), and purified sample solutions were stored in acid-cleaned polyethylene (LDPE) VWR metal-free centrifuge tubes. All equipment was handled with polyethylene gloves using trace metal clean practices. Before use, batches of Nobias-PA1 resin were cleaned in 3 M nitric acid for >1 day and rinsed with ultrapure water. Likewise, AG-MP1 resin was cleaned in 10% hydrochloric acid solution and stored in ultrapure water until use (Conway et al., 2013).

2.3. Sample pretreatment and concentration analysis

Seawater samples (1L) were acidified to pH = 1.8 with 1 mL concentrated distilled HCl, and left acidified for at least a month. Samples for concentration analysis were aliquoted into 15 mL acid-washed centrifuge tubes and amended with 50 μ L of an isotope spike containing ⁵⁷Fe, ⁶²Ni, ⁶⁵Cu, ⁶⁷Zn, and ¹¹⁰Cd. Metals were extracted onto Nobias PA-1 resin using a SeaFAST preconcentration system (Elemental Scientific) and eluted into 1.5 M nitric acid containing 1 ng mL⁻¹ In. Extracted metals were analyzed by inductively coupled plasma mass spectrometry (ICP-MS) on an Element 2 Instrument (Thermo) at the University of Southern California. Detailed information regarding the methods, data calibration, blank correction and verification were described in Hawco et al. (2020).

For particulate samples, each 47 and 142 mm-diameter filter was digested by placing the filter in a 25 mL acid-washed PFA vial containing 5 mL of 8 M HNO₃

(HF was deliberately not used to digest the samples in order to minimize the decomposition of lithogenic materials). Samples were digested in capped vials on a hot plate at 120 °C for 12 h (Cullen and Sherrell, 1999). After digestion, the filters were taken out, placed into acid-washed 15 mL centrifuge tubes and rinsed with 5 mL Milli-Q water. The Milli-Q water was transferred into the same digestion vials. The digest solution was then heated on a hot plate at 80 °C to dryness. Dried down samples were then re-dissolved by adding 10 mL of 4 M HNO3, transferred into acidwashed 15 mL centrifuge tubes, and centrifuged at 2000 rpm for 5 mins to segregate insoluble particles and filter debris. A small portion of supernatant was taken into acid-washed 15 mL centrifuge tubes, diluted by 10 times and amended with In standard solution with matrix of 0.1 M nitric acid to reach a final concentration of 1 ng mL⁻¹ In. The diluted samples were analyzed for Ni, P, Fe, Mn and Ti concentrations on an Element XR Instrument (Thermo) at the Research Center for Environmental Changes, Academia Sinica, Taiwan, following the analytical settings and protocol in Yang et al. (2020).

2.4. Ni preconcentration for isotope analysis

Before preconcentration, a 61Ni-62Ni double spike was added to acidified seawater and centrifuged particle digests to achieve a spike to sample ratio of ~1:1 (mol:mol). Spiked seawater samples were left to sit for at least three days in order for the sample and spike to equilibrate. Ni in both types of samples were then extracted using the protocol established in Yang et al. (2020). Briefly, a slurry of 2.5 mL pre-cleaned Nobias PA1 resin was added to 1 L pH = 1.8 seawater and shaken overnight on a shaker table. The pH of the solution was adjusted to 6.0 ± 0.2 by adding an ammonium acetate buffer and shaking the samples for ~5 h. Afterward, the resin was filtered from the solution using an acid-washed 8 µm polycarbonate filter (Whatman), rinsed thoroughly with Milli-Q water and eluted in ~20 mL of 3 M nitric acid. Both seawater Ni extracts and spiked particle digests were evaporated to dryness, redissolved in 0.5 mL 15 M acetic acid +1.2 M HCl and further purified.

Ni was separated from other metals that have the potential to interfere with isotopic analysis by adding the samples dissolved in 15 M acetic acid + 1.2 M HCl to 0.25 mL of wet AG-MP1 (100–200 mesh) anion exchange resin situated in Bio-Spin® Disposable Chromatography Columns (no. 7326008) and eluting the Ni with 15 M acetic acid + 1.2 M HCl. The eluent was then dried down, redissolved in 0.5 mL 0.05 M ammonium acetate (pH = 6), and then purified by pouring the samples through 0.6 mL of Nobias-PA1 resin (wet volume) situated in the same type of columns. The Nobias resin was then rinsed with ammonium acetate and Ni was eluted from the resin with 1 M nitric acid. Lastly, the eluent was purified again by using the same Ni separation procedure that includes the AG-MP1 resin. After purification, the Ni elution fractions were collected and evaporated to dryness in 7 mL PFA vials, then refluxed in 1 mL of 14 M HNO₃ and 0.1 mL of 35% H₂O₂ at 160 °C for at least 6 hours to decompose any

leftover organic matter (Yang et al., 2020). The samples were finally evaporated to dryness again and re-dissolved in 0.1 M HNO₃ to achieve a final concentration of approximately 200 ng mL⁻¹ Ni. The overall recovery efficiency ranged from about 70–100% obtained from beam matching between samples and standards of known concentration during Ni isotopic analysis.

2.5. Blanks

Overall procedural blanks for Ni analysis (including full Nobias-PA1 extraction, Ni separation and purification) were <1 ng Ni. Compared to the Ni masses of samples we processed (130-490 ng for seawater, 450-3200 ng for particles between the 0.8 and 51 µm size range, and 38-1900 ng for particles >51 µm) this blank is negligible, and so no procedural blank correction of Ni isotope ratios was made. However, for particle samples, the Supor polyethersulfone filters (for particles between 0.8 and 51 μm) and Sefar polyester filters (for particles >51 μm) themselves can be relatively significant sources of Ni contamination. Blank filters treated with the same digestion protocol as the sample filters presents on average 3.3 ± 2.4 ng Ni (1 σ and n = 3) for Super polyethersulfone filters and 5.8 \pm 2.4 ng Ni (1 σ and n = 4) for Sefar polyester filters. However, this amount still corresponds to only 0.1– 0.7% and 0.2-2.2% of the Ni in the 0.8-51 and >51 µm particle samples, respectively, with two exceptions of >51 μm samples collected at 15 m (6.8%) and 25 m (8.7%), which are noted below in our interpretation of isotopic results from these samples.

2.6. Ni isotopic analysis

The isotopic composition of Ni (δ^{60} Ni) in the ODZ samples were measured on a Thermo Neptune Plus MC-ICPMS in the Tampa Bay Plasma Facility at the University of South Florida or at the Institute of Earth Sciences (IES), Academia Sinica, Taiwan. In both cases, jet sampler and 'x-type' skimmer cones were used to maximize sensitivity and all standards and samples were introduced through a $100-150~\mu L~min^{-1}$ Teflon nebulizer using an Apex-Q desolvating system (Elemental Scientific).

The instrumental settings and data acquisition method used in this study were taken from Yang et al. (2020). Briefly, four Ni isotopes, ⁵⁸Ni, ⁶⁰Ni, ⁶¹Ni and ⁶²Ni, were simultaneously measured in 'high resolution' mode in each analysis, along with ⁵⁷Fe to correct isobaric interference on ⁵⁸Fe. Data collection consisted of 30 cycles, each 4.2 s long. Pure 0.1 M HNO₃ solution was measured between every 4-6 samples to determine background signals that the average of each two analyses were then subtracted from intensities of the samples between them. The primary standard NIST 986 Ni was also measured routinely, between every 4-6 samples, to correct for potential systematic drift during each session. A double spike data reduction scheme following the iterative approach of Siebert et al (2001) was used to correct the artificial isotopic fractionation on sample Ni potentially caused by purification protocols and mass spectrometry. Isotope ratios are expressed in permil (%) relative to the average of the two NIST 986 Ni analyses around each block of 4–6 samples, using delta notation calculated as following;

$$\delta^{60}Ni = \left[\frac{\left({}^{60}Ni / {}^{58}Ni \right)_{sample}}{\left({}^{60}Ni / {}^{58}Ni \right)_{NIST\ SRM\ 986}} - 1 \right] \times 10^{3}$$

The accuracy of our analytical technique was verified by determining the isotope composition of a secondary standard on the same day at IES. Wako Ni was measured to be $-0.31 \pm 0.07\%$ (2σ , n = 6), which is consistent with the values reported by Yang et al. (2020).

Long-term reproducibility of Ni isotope analyses is $\pm 0.08\%$ (n=21; over ~ 1 year), which was assessed over the course of this and parallel studies through repeated measurements of NIST 986 and a secondary standard Wako Ni at IES. The internal precision of single measurements typically ranged from ± 0.02 to $\pm 0.07\%$, which was obtained by combining the internal precision of both sample and standard measurements (Conway et al., 2013). Only two particulate samples were less precise ($\geq \pm 0.20\%$) due to low sample mass. The reported analytical reproducibility for the isotopic composition of each sample is the long-term reproducibility, unless the internal uncertainty is larger, in which case the latter is reported.

3. RESULTS

3.1. Dissolved Ni concentrations and isotopic composition

3.1.1. 2018 cruise

Dissolved Ni concentrations and δ^{60} Ni of seawater (Fig. 3) collected on the 2018 cruise exhibit similar vertical patterns at all four stations, in both the ODZ and suboxic regions, despite there being drastic differences in oxygen, nitrite and chlorophyll a (Chl a) concentrations (Fig. 2). At all stations, the Ni concentrations increase roughly three-fold (from 2.8 to 8.4 nmol kg⁻¹) and the isotopic composition declines by 0.2% (from +1.6 to +1.4%) with depth (from 0 to 700 m; Fig. 3). In detail, the vertical variations in dissolved Ni seem to reflect three different concentration gradients: a sharp increase from 3 to 4 nmol kg⁻¹ in the top 75 m which is mainly composed of ESW, a moderate increase from 4 to 5.5 nmol kg⁻¹ from 75 to 300 m where 13CW is located, and then a more rapid increase from 5.5 to 8 nmol kg⁻¹ from 300 to 700 m where NEPIW and AAIW are located. The difference in measured δ^{60} Ni between various depths is similar to the magnitude of the analytical uncertainty, yet when considered together a clear pattern of decreasing δ^{60} Ni with increasing depth emerges, with δ^{60} Ni of +1.55 \pm 0.02‰ (2 $\sigma_{\rm m}$ which stands for 2 σ of the mean, $2\sigma/n^{0.5}$; n = 21) in the top 75 m, $+1.44 \pm 0.01\%$ $(2\sigma_{\rm m}, n = 39)$ from 75 to 300 m, and $+1.39 \pm 0.02\%$ $(2\sigma_{\rm m}, n = 39)$ n = 13) below 300 m.

3.1.2. 2017 pilot cruise

During the December 2017 cruise seawater samples were collected at five depths each at two stations within the ODZ (Stations P1 and P2) and were analyzed for Ni

concentrations and $\delta^{60}Ni$. Combined with data from 2018, we can therefore use our dataset to explore possible temporal variations. In 2017 the maximum Chl a concentrations were seventeen times higher than the max Chl a concentrations in 2018 (34.2 $\mu g L^{-1}$ vs. 2.0 $\mu g L^{-1}$; Fig. 2). Despite the large differences in primary productivity, Ni concentrations and δ^{60} Ni were quite similar between the two cruises (2017 and 2018) (Fig. 3). The 2017–2018 difference in chlorophyll a was less dramatic at station P2, with the Chl a maximum about three times higher in 2017 than in 2018 (2.9 μ g L⁻¹ vs. 1.0 μ g L⁻¹; Fig. 2). The Ni concentrations in ESW and NEPIW were 0.6-0.8 nmol kg⁻¹ lower in 2017 than in 2018 (Fig. 3). In addition, the heaviest δ^{60} Ni in this study (+1.69 \pm 0.07‰) was found in ESW in 2017, which is about 0.14% heavier than δ^{60} Ni from the same depth and location in 2018. However, when we compare Ni concentrations and δ^{60} Ni as a function of seawater density instead of depth, all of the data from 100 to 600 m in both 2017 and 2018 align well with each other (Fig. 4), suggesting that the temporal differences observed at P2 were due to slight differences in the vertical position of key water masses. The surface water sample from station P2 which had the heaviest dissolved δ^{60} Ni also had the lowest density (~22.4; Fig. 4), suggesting the presence of a different water mass carrying a unique Ni isotopic signature.

Nickel concentrations and δ^{60} Ni within the 'soluble' phase (sometimes referred to as 'truly dissolved', <0.02 µm) were also measured for 5 samples from station P2. Soluble Ni (<0.02 µm) concentrations and δ^{60} Ni values overlap with the data for total dissolved Ni (<0.2 µm) (Fig. 3), indicating that there is little Ni in the colloidal size range (0.02–0.2 µm) and any colloidal Ni which does occur has a similar δ^{60} Ni signature.

3.2. Particulate Ni concentrations and isotopic composition

Particle samples collected at station P1 in 2018 show very different patterns of Ni concentration and δ^{60} Ni compared to the dissolved phase. Nickel concentrations in the total suspended particles filtered from seawater (>0.2 µm) exhibit a maximum value of 214 pmol kg⁻¹ at 15-20 m where the chlorophyll a maximum is located (Fig. 5). Samples from the McLane pumps provided particles both in the $0.8-51 \mu m$ and $>51 \mu m$ size ranges, with approximately one third of the Ni occurring the >51 µm size range below the Chl a maximum, and up to half the Ni in the >51 um size range within the Chl a maximum (15–20 m; Fig. 5). By comparing total suspended particles (>0.2 µm) with the sum of particles in the 0.8–51 μ m and >51 μ m size ranges, we can infer the concentration of elements in the 0.2–0.8 µm size range. At least half or more of the phosphorus (P) was always observed in the 0.2–0.8 µm range, yet most of the Ni was found in particles >0.8 µm (Fig. 5). The exception to this was at the Chl a maximum, where most of the Ni (roughly three quarters) occurred in the 0.2-0.8 µm size range. At 50 m, the combined Ni concentrations from the $0.8-51 \mu m$ and $>51 \mu m$ particles are three times higher than the total suspended particles concentration (>0.2 µm), which is likely due to contamination, and thus these

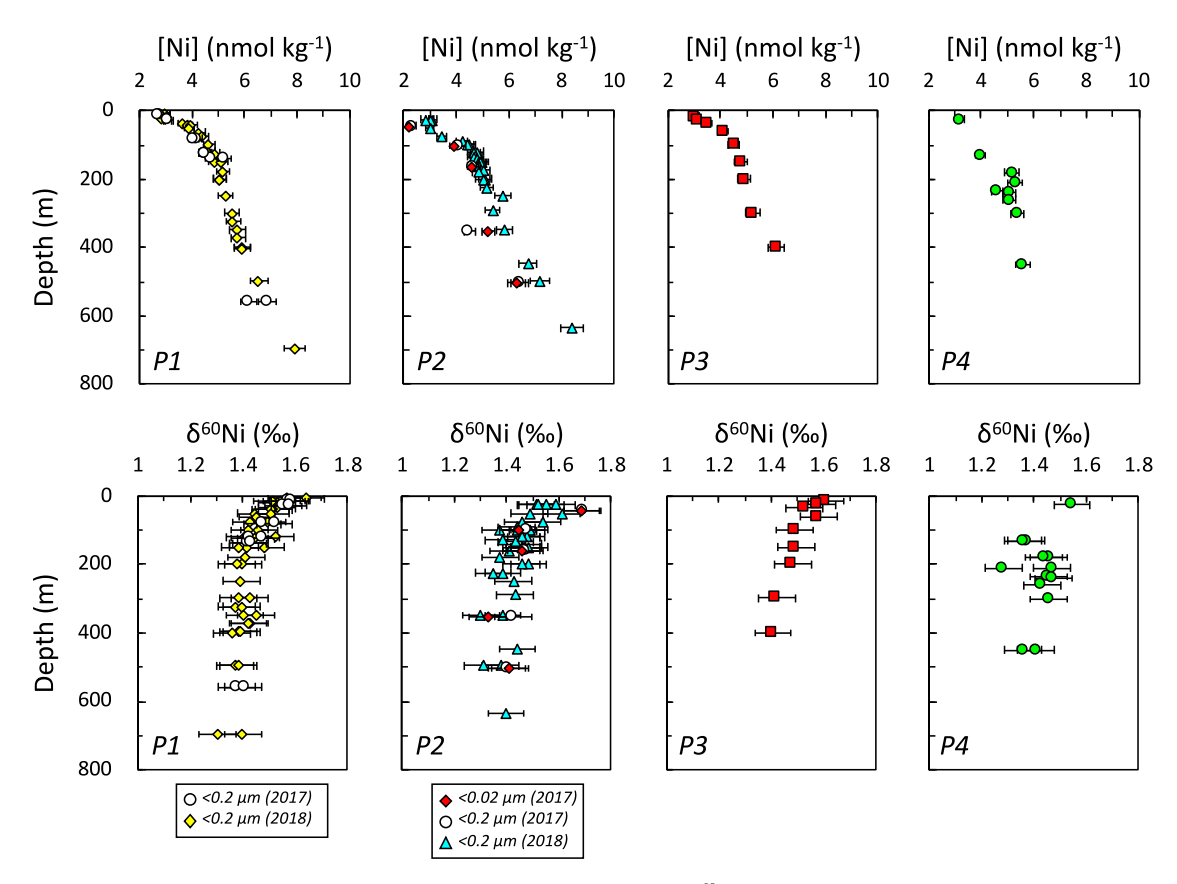


Fig. 3. Depth profiles of dissolved Ni concentrations and isotopic composition (δ^{60} Ni) at the ODZ stations P1 (yellow diamonds), P2 (blue triangles), P3 (red squares) and a suboxic station P4 (green circles) during the 2018 expedition, along with depth profiles of dissolved Ni at P1 and P2 (open circles) and soluble Ni (<0.02 μ m) at P2 (red diamonds) during the 2017 cruise. Error bars denote long-term reproducibility (2 σ) of concentration and isotopic analyses, $\pm 5\%$ and $\pm 0.08\%$, respectively. (For interpretation of the references to color in this figure legend, the reader is referred to the web version of this article.)

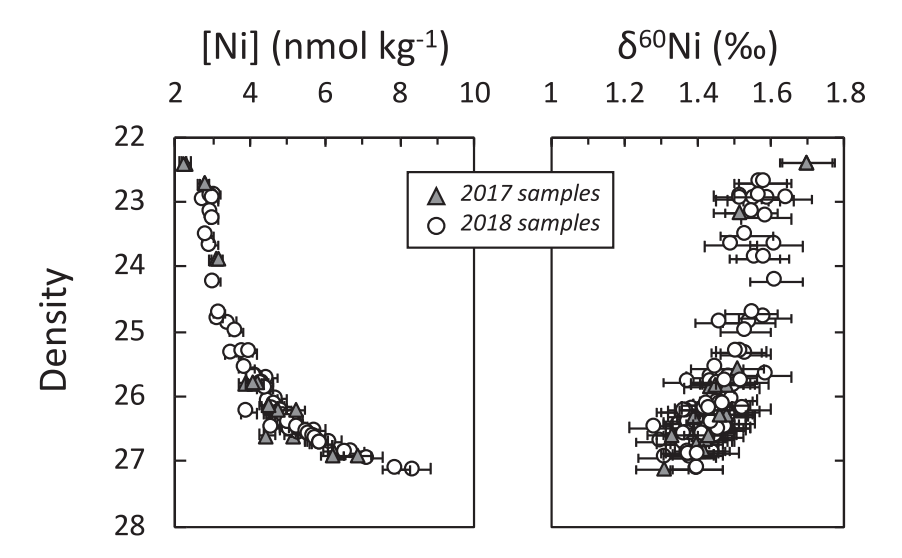


Fig. 4. Dissolved Ni concentrations and isotopic composition compared to density for the samples collected in 2017 (gray triangles) and 2018 (open circles) at ODZ stations P1 and P2.

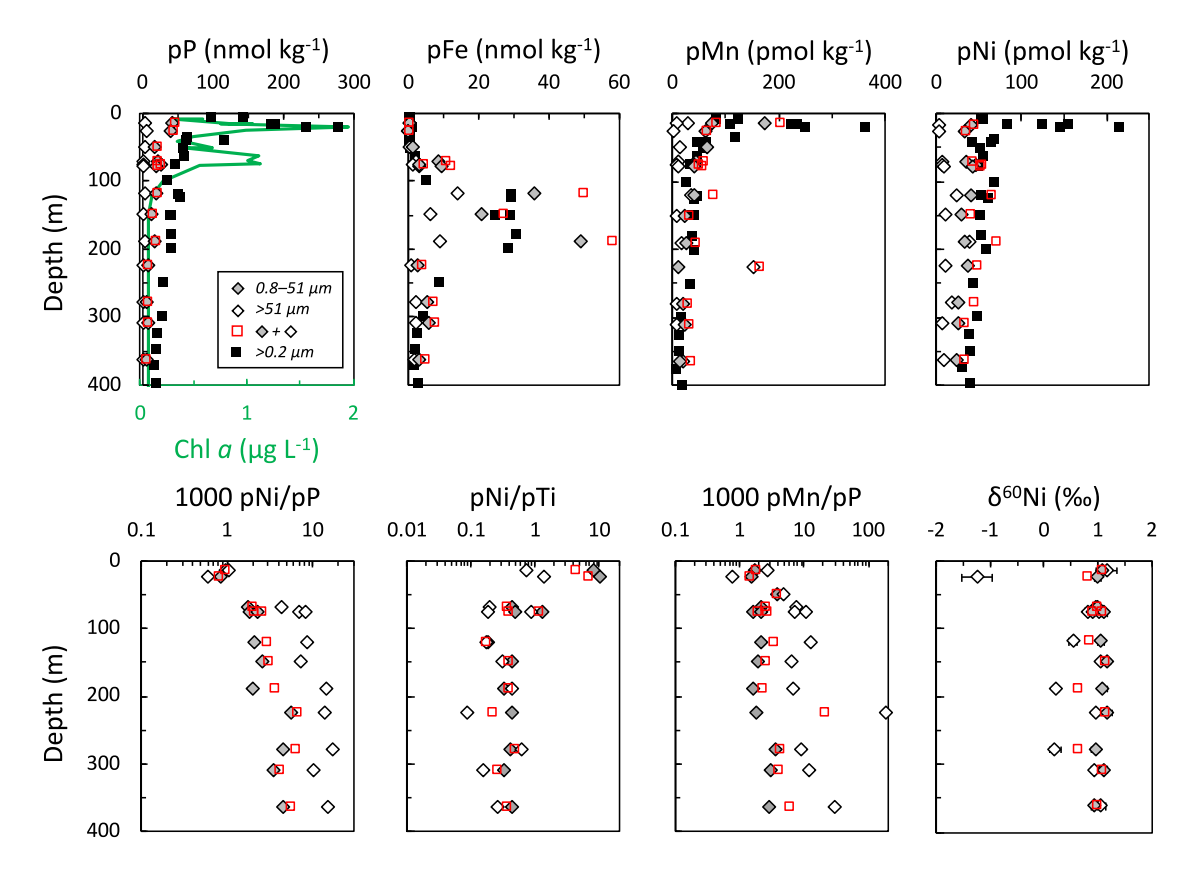


Fig. 5. Concentrations of particulate P (pP), Fe (pFe), Mn (pMn), Ni (pNi), Ni isotopic composition (δ^{60} Ni), elemental ratios (including pNi/pP multiplied by 1000, pNi/pTi, and pMn/pP multiplied by 1000), and concentrations of chlorophyll *a* (Chl *a*) throughout the water column at station P1 in 2018. Filled squares represent total suspended particles ($>0.2~\mu$ m) collected by onboard filtering of seawater. Open and gray diamonds stand for particles with sizes of $0.8-51~\mu$ m and $>51~\mu$ m, respectively, collected from submerged McLane pumps. Red open squares represent the sum of the two McLane pump size fractions ($>0.8~\mu$ m). (For interpretation of the references to color in this figure legend, the reader is referred to the web version of this article.)

samples are not discussed further (see data in Supplementary Appendix B).

Particulate δ^{60} Ni values are consistently lower than dissolved δ^{60} Ni, by between 0.4 and 2‰, and have a variability three to four times that of dissolved δ^{60} Ni. Particulate δ^{60} Ni values range from +0.1 to +1.2‰ in >0.8 µm particles, with the exception of a single >51 µm sample collected at 25 m (-1.24 \pm 0.28‰; Fig. 5). In 0.8–51 µm particles, δ^{60} Ni is fairly consistent throughout all twelve samples and ranges from +0.9 to +1.2‰ (data from 50 m is excluded). Most δ^{60} Ni values from >51 µm particles are similar to 0.8–51 µm particles, except for four samples which are obviously lighter (-1.24 to +0.54‰).

4. DISCUSSION

The Ni concentration and isotope values obtained in this study allow us to evaluate several hypotheses about Ni biogeochemical cycling. The δ^{60} Ni observations are first explored using three different theoretical frameworks: 1) passive mixing between water masses, 2) biological fractionation and Rayleigh distillation, and 3) biological fractionation and Rayleigh distillation in a two-phase system with

both bioavailable and non-bioavailable Ni. These frameworks are used to help identify which biogeochemical processes may affect Ni cycling in our study region. We first examine just the dissolved phase Ni and δ^{60} Ni data, then explore what additional insight can be gained from particulate δ^{60} Ni data. Next, we consider how the unique characteristics of our study site, especially the presence of an intense open-ocean ODZ and active Mn cycling do or do not affect Ni cycling. Finally, we put our data within the context of global dissolved Ni/ δ^{60} Ni datasets in order to understand global controls on Ni and Ni isotope cycling.

4.1. Physical circulation and mixing

Away from the surface ocean, advection and mixing of seawater are dominant processes controlling the distributions of dissolved Ni (e.g. Middag et al., 2020), and these physical processes also clearly affect the distributions of dissolved Ni and $\delta^{60}Ni$ in the ETNP. While slight differences are observed between the dissolved Ni and $\delta^{60}Ni$ profiles at stations P1-P4 when plotted as a function of depth (Fig. 3), both Ni and $\delta^{60}Ni$ from all four stations align well when plotted against density (Fig. 4). This suggests that

many of the differences seen between stations are the result of slight changes in the vertical dominance of the key water masses of the region.

Furthermore, the variations in the dissolved Ni and δ^{60} Ni between the key water masses can be well described by conservative binary mixing. This model assumes mass balance of Ni concentration and isotopes:

$$[Ni]_1 f_1 + [Ni]_2 f_2 = [Ni]_{mixed}$$

$$d^{60}Ni_1 [Ni]_1 f_1 + d^{60}Ni_2 [Ni]_2 f_2 = d^{60}Ni_{mixed} [Ni]_{mixed}$$

$$f_1 + f_2 = 1$$

where [Ni], δ^{60} Ni and f stand for dissolved Ni concentration, dissolved δ^{60} Ni and volume fraction for each pair of adjacent water mass endmembers, respectively. Endmember water masses and their dissolved [Ni] and δ^{60} Ni were identified according to their temperature and salinity as follows: ESW (21.3–23.3 °C and 34.3 psu), 13CW (12.5–13.1 °C and 34.8 psu), NEPIW (~9.6 °C and 34.6 psu) and AAIW (~6.0 °C and 34.5 psu) (Fig. 1; Supplementary Appendix A). Averaged dissolved [Ni] and δ^{60} Ni for each endmember are thus: ESW (3.0 nmol kg⁻¹ and +1.55‰), 13CW

(4.8 nmol kg $^{-1}$ and +1.44‰), NEPIW (6.0 nmol kg $^{-1}$ and +1.39‰) and AAIW (8.2 nmol kg $^{-1}$ and +1.33‰). This physical mixing model yields [Ni] $-\delta^{60}$ Ni patterns

This physical mixing model yields [Ni]– δ^{60} Ni patterns which are consistent with our observations in the ETNP (Fig. 6A). Indeed, physical mixing may be the predominant control on δ^{60} Ni distributions, especially in the deep ocean. However, while water movement and mixing of water masses can explain the distributions of both the dissolved [Ni] and δ^{60} Ni in the ETNP, they cannot explain why the water masses possess distinctly different "pre-formed" concentrations and isotopic compositions in the first place. In the following section, we consider the other process important to Ni cycling— biological uptake, whether *in situ* or earlier in the transport pathway of each water mass.

4.2. Biological fractionation of Ni isotopes by Rayleigh distillation

The major water masses in the ETNP can be traced back to the Southern Ocean (Fiedler & Talley, 2006; Evans et al., 2020), and we thus expect that some of the variability in

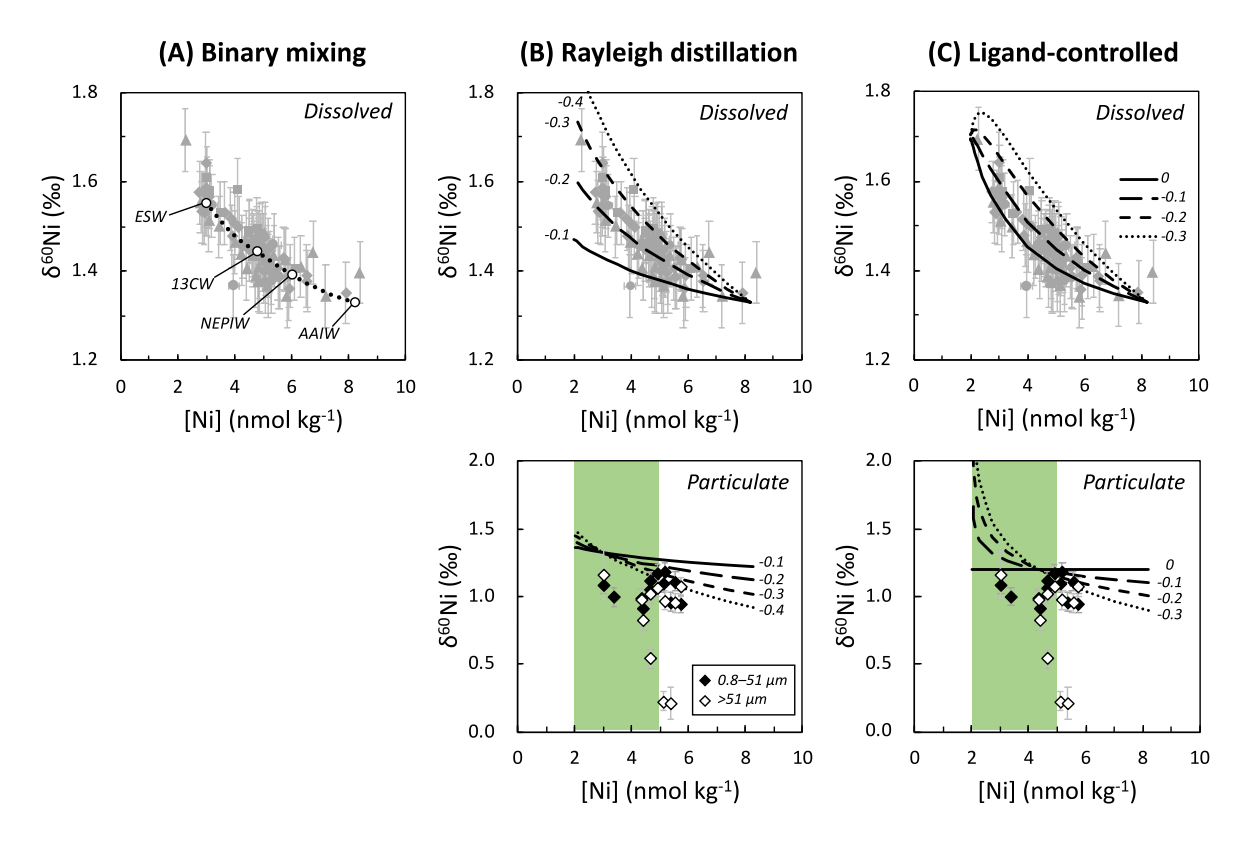


Fig. 6. Comparison of dissolved and particulate Ni isotopic composition $(d\delta^{60}Ni)$ and $p\delta^{60}Ni)$ versus Ni concentrations (dNi) of samples collected in this study. Isotope systematics can be modeled as simple physical mixing between water masses, where open circles represent the dNi and $d\delta^{60}Ni$ at the depths where ESW, 13CW, NEPIW and AAIW values converge, and dashed lines between the open circles are derived from a conservative binary mixing model (A). Alternatively, the data can be modeled by Rayleigh distillation, with the data suggesting an instantaneous isotope effect ($\Delta^{60}Ni_{particulate-aqueous}$) of -0.1 to -0.4% (B). Finally, the data can be fit by a Rayleigh fractionation model which assumes 2 nM of non-bioavailable Ni with a $\delta^{60}Ni$ value of +1.7%, and isotope effects from 0 to -0.3% (C). In all plots, the gray symbols show observations from this study. For both Rayleigh models, we show the predicted instantaneous $\delta^{60}Ni$ of phytoplankton export, compared to observed particle $\delta^{60}Ni$ in the 0.8–51 µm (filled diamonds) and >51 µm size (open diamonds) ranges, respectively. Green shaded areas show the concentration range of dissolved [Ni] in the euphotic zone (top 100 m). A value from a >51 µm particle sample at 25 m was identified an outlier, and is therefore not included here.

dissolved [Ni] and δ^{60} Ni can also be traced back to biological uptake (and regeneration) in the Southern Ocean and the waters flowing northwards. To quantify the proportion of Ni removed by biological uptake and therefore the degree of Ni isotopic fractionation, a closed system Rayleigh fractionation model is applied as a conventional approach. This model assumes that the dominant source of Ni in the upper ocean is from a constant deep Ni pool, and that the main process controlling dissolved [Ni] and δ^{60} Ni distributions in both the upper and deep oceans is phytoplankton uptake of light Ni isotopes followed by removal by subsequent settling, microbial degradation and release of Ni at depth. A theoretical relationship of dissolved [Ni] and δ^{60} Ni between the upper ocean and the global deep Ni pool can be expressed as the following:

$$\delta^{60}Ni = \Delta^{60}Ni_{\mathrm{particulate-aqueous}}\hat{\mathbf{A}} \cdot ln\left(\frac{[Ni]}{[Ni]_0}\right) + \delta^{60}Ni_0$$

where [Ni]₀ and δ^{60} Ni₀ denote the concentration and isotopic composition of dissolved Ni of the deep Ni pool, [Ni] and δ^{60} Ni for the upper ocean, and Δ^{60} Ni_{particulate-aqueous} for the biological isotopic fractionation.

Applying AAIW δ^{60} Ni and Ni concentrations as calculated above (Section 4.1) to [Ni]₀ and δ^{60} Ni₀ of the equation, the application to our ETNP Ni dataset yields a δ^{60} Ni–Ni relationship (Fig. 6B):

$$d^{60}Ni = -0.23(\pm 0.03) \cdot \ln[Ni] + 1.81(\pm 0.05); R^2 = 0.71$$

Using Ni concentrations for all water masses (Section 4.1), the estimated dissolved δ^{60} Ni of ESW, 13CW and NEPIW would be $+1.56\pm0.03$, $+1.45\pm0.05$ and + $1.40 \pm 0.05\%$, respectively. These modeled dissolved δ^{60} Ni values also match observations well, thus it is possible that closed system Rayleigh fractionation can explain the distinct dissolved [Ni] and δ^{60} Ni found in each water mass. The slope of the equation reflects the biological isotopic fractionation, $\Delta^{60}Ni_{particulate-aqueous}$, and is equal to $-0.23 \pm 0.03\%$ (2 σ), meaning that co-evolution of dissolved [Ni] and δ^{60} Ni during the formation and transport of the water masses is driven by an instantaneous isotopic difference of $-0.23 \pm 0.03\%$ between phytoplankton and the dissolved pool. The fractionation is consistent with the subtropical North and South Pacific and the South Atlantic ($-0.27 \pm 0.03\%$ to $-0.28 \pm 0.07\%$; estimated from datasets in Takano et al., 2017, Archer et al., 2020; Yang et al., 2020).

Analyses of particulate δ^{60} Ni can be compared to these dissolved data in order to better understand the magnitude of biological fractionation in the ETNP ODZ. Measured δ^{60} Ni in 0.8–51 µm and >51 µm particles in the euphotic zone (top 100 m) at station P1 are lighter than the dissolved phase by 0.50 \pm 0.08‰ (1 σ and n=5) and 0.52 \pm 0.11‰ (1 σ and n=4), respectively (Fig. 5). This supports the assumption that biological uptake of light Ni drives variations in dissolved [Ni] and δ^{60} Ni in the ocean, but is slightly larger than the Δ^{60} Ni particulate-aqueous of -0.23‰ suggested by simple Rayleigh distillation (Fig. 6B).

The inconsistency between observed $\Delta^{60}Ni_{particulate-aqueous}$ and the biological isotope effect suggested by a Rayleigh

distillation model may suggest that simple Rayleigh distillation is not the only process controlling [Ni] and δ^{60} Ni. Exchange and mixing between water masses may decrease the δ^{60} Ni values and the gradient of the δ^{60} Ni–Ni relationship produced by biological uptake. ETNP surface water is mainly composed of ESW, originating from a mixture of upwelled waters and the Equatorial Undercurrent, and PSUW, carried by the California Current (Evans et al., 2020), and thus δ^{60} Ni signatures likely reflect a mixture of the isotopic signatures of these two currents. Additionally, particulate δ^{60} Ni may represent biological fractionation at a single point in time which is not reflective of the time history of biological activity. Primary productivity and community structures in the ETNP fluctuate daily (Almazán-Becerril and García-Mendoza, 2008), and various phytoplankton species have different Ni demands (Twining et al., 2012; Ho et al., 2013; Rodriguez and Ho, 2014) and biological Ni isotope fractionations (Cameron et al., 2009). Biological Ni uptake and perhaps Ni isotopic fractionation effects may therefore be highly dynamic. Indeed, analyses of δ^{60} Ni in sinking particles in the deep northern South China Sea also show temporal variations as much as 0.6% within one year (Takano et al., 2020), which may be associated with the seasonally dynamic community structures in the surface ocean (Ho et al., 2015).

An alternative explanation for the inconsistency between Rayleigh-predicted Δ^{60} Ni_{particulate-aqueous} and observations is that particles are also influenced by partial dissolution of accompanying lithogenic material with a δ^{60} Ni of $+0.15 \pm 0.06\%$ (1 σ) (Elliott and Steele, 2017). However, this explanation is not supported by the Ni/P ratios of the particles, which appear similar to biological ratios: euphotic zone particle Ni/P ratios measured here range from 0.9 to 8.2 mmol mol⁻¹, which is within or slightly higher than the range found in various plankton lab cultures and in the natural surface ocean community (0.07-3.3 mmol mol⁻¹; e.g. Ho, 2013; Twining et al., 2012, 2014). Additionally, particulate Ni/Ti ratios, an indicator of the contribution of Ni from lithogenic material, showed that lithogenic Ni in the particles was negligible, despite the sampling site being nearshore and only about 70 km away from the Ameca River estuary. The Ni/Ti ratio of particle samples from the top 100 m ranged between 0.18 and 10 mol mol⁻¹, which is one to four orders of magnitude higher than the ratio found in upper crustal materials (0.0 02-0.029 mol mol⁻¹; estimated from data in Wedepohl, 2000). Thus, we conclude that the particulate δ^{60} Ni signatures likely reflect local biological fractionation at the time of sampling.

4.3. Biological fractionation of Ni with a non-bioavailable pool

Nickel is never drawn much below 2 nmol kg⁻¹ throughout the global surface ocean, leading to the suggestion that dissolved Ni may be comprised of separate bioavailable and non-bioavailable pools (Mackey et al., 2002; Archer et al., 2020; Boiteau et al., 2016). A 2 nmol kg⁻¹ non-bioavailable pool may be attributed to strong complexation with organic ligands (Mackey et al., 2002; Dupont et al.,

2010), coupled with slow coordination kinetics of phytoplankton Ni uptake (Hudson and Morel, 1993; Dupont et al., 2012) that prevents complete drawdown of Ni. Considering the effects of ligand complexation on Ni availability, Archer et al. (2020) hypothesized that non-bioavailable and bioavailable Ni pools possess distinct δ^{60} Ni signatures, comprised of roughly 2 nmol kg⁻¹ non-bioavailable Ni with δ^{60} Ni = +1.7‰, a deep-ocean bioavailable pool with δ^{60} Ni = +1.2‰, and limited isotopic exchange between these pools. Dissolved δ^{60} Ni data from the South Atlantic is consistent with this model and either no biological fractionation during uptake, or a small fractionation of -0.12‰ (Archer et al, 2020).

The same model provides a good fit to our data. Assuming 2 nmol kg⁻¹ of non-bioavailable Ni with a δ^{60} Ni value of +1.7‰, and the remainder of Ni is bioavailable and has a starting δ^{60} Ni of +1.2‰, best fits are obtained with small biological fractionations of around -0.1‰ (Fig. 6C).

As with the simple Rayleigh model (Section 4.2), the predicted offset between dissolved and particulate δ^{60} Ni is smaller than observations, and this inconsistency can be attributed to the same processes discussed above including temporal or spatial variability in phytoplankton communities with different biological isotope effects. Intriguingly, however, the two models suggest very different particulate δ⁶⁰Ni when bioavailable Ni becomes nearly depleted (Fig. 6B and C): in the absence of a non-bioavailable Ni pool (simple Rayleigh distillation) particulate Ni does not change much as Ni is depleted, while in the presence of a non-bioavailable pool the particles are formed from a residual bioavailable pool which is becoming very highly fractionated by Rayleigh distillation, and thus both the residual bioavailable dissolved phase δ^{60} Ni and the particulate δ^{60} Ni are expected to become much heavier. We therefore suggest future investigations should pursue analysis of particulate δ⁶⁰Ni in regions where surface-ocean Ni becomes more depleted to nearer 2 nmol kg⁻¹ such as western tropical/subtropical Pacific and Atlantic Oceans (e.g. Mackey et al., 2002; Middag et al., 2020).

4.4. Ni isotope cycling within ETNP oxygen deficient waters

The Eastern Tropical North Pacific (ETNP) studied here is the largest ODZ worldwide, of similar scale as ODZs in the northern Indian Ocean and the Eastern Tropical South Pacific (ETSP). Our samples thus provide a unique opportunity to see how such low-oxygen conditions affect Ni cycling.

At present, the redox threshold where metal sulfide precipitation becomes a significant effect remains poorly understood. In the deep Black Sea, where sulfide concentrations build up to micromolar levels, the precipitation of Ni sulfides is thought to be a significant sink for Ni, with a preferential loss of lighter Ni isotopes (Δ^{60} Ni_{particulate-aqueous} = -0.7%; Vance et al., 2016). In the open ocean where measurable sulfide is not present, it has been suggested that extremely reducing conditions within organic-rich particles could lead to sulfide production and precipitation of metal sulfides (e.g. Janssen et al. 2014, Bianchi et al., 2018). However, our dissolved data

shows no obvious evidence of Ni sulfide formation in the ETNP. In fact, as discussed above (Section 4.1) the subsurface dissolved Ni and δ^{60} Ni patterns can be described by mixing between water masses, without any obvious deviations attributable to low-oxygen conditions.

Similarly, ETNP particle Ni isotope systematics can be mostly attributed to biological processes in the surface ocean. All of the 0.8-51 µm samples and four of the seven >51 µm samples below the euphotic zone show δ^{60} Ni values that vary only within a 0.3% range and have values that are consistent with the δ^{60} Ni in the euphotic zone (ranging from ± 0.9 to $\pm 1.2\%$) (Fig. 5). This consistency suggests that the particles below the euphotic zone largely inherit the isotopic signature from the surface ocean, rather than being impacted by processes at ODZ depths. That said. while most of the particle samples are consistent with phytoplankton detritus (all of the 0.8-51 µm samples and over half of the >51 µm samples below the euphotic zone), three >51 µm samples do possess lighter δ^{60} Ni values $(+0.21 \pm 0.11 \text{ to } +0.54 \pm 0.07\%)$ and have Ni/P ratios higher than neighboring samples (Fig. 5). These particles are 0.4–1.0% lighter than the particles in the euphotic zone, 0.9-1.2% lighter than the ambient seawater, and they seem to match the isotope effect observed in the sulfidic deep Black Sea. In our samples, the lighter δ^{60} Ni values in these few samples could alternatively be explained by more lithogenic Ni, since this would be expected to be lighter than both seawater and marine particles (~+0.1%, Cameron et al., 2009; Hawco et al., 2020). Indeed, Takano et al. (2020) previously showed that lithogenic Ni has significant impacts on deep-sea sinking particles in the northern South China Sea. Several of their samples possess δ^{60} Ni values that are ~1.5\% lighter than seawater and have low Ni/Ti ratios that are close to the Ni/Ti ratios of upper crustal materials (Takano et al., 2020). However, addition of lithogenic Ni is considered less likely for our open-ODZ particles because of sampling technique: while HNO₃ and HF were both used in the sample digestion in Takano et al. (2020), only 8 M HNO₃ was used here to minimize the decomposition of lithogenic materials. Using this method, our particles show Ni/Ti ratios (0.09–0.61 mmol mol⁻¹) that are 3-300 times higher than lithogenic Ni/Ti ratios $(0.002-0.029 \text{ mol mol}^{-1})$. Additionally, δ^{60} Ni values do not shift toward ~+0.1% when Ni/Ti ratios are low (Fig. 5).

The ETNP is also a region with an active dissolvedparticle redox cycle involving both Fe and Mn oxides, as both elements cycle between the dissolved phase (in lowoxygen waters) and particle phase (when mixed into more oxygenated waters). Consequently, dissolved and particulate Mn concentrations in the ETNP are much higher than typical open-ocean concentrations of <~100 pmol kg⁻¹ (e.g. Lee et al., 2018), with active Mn particle dissolution in the ETNP ODZ visible in low-oxygen waters (100-250 m) as decreased Mn:P in the 0.8-51 µm particles, and elevated dissolved Mn concentrations (Figs. 2 and 5). Particulate Fe concentrations also increase dramatically between 100 and 250 m, which coincides with the nitrite maximum (Figs. 2 and 5). Similar co-occurring particulate Fe and nitrite peaks have be observed at inshore stations in the Peruvian ODZ and were determined to be a result of the combined effects of dissimilatory reduction of Fe in shelf sediments, lateral transport of dissolved Fe(II), and formation of Fe oxyhydroxides particles (Heller et al., 2017).

Particulate Ni below the euphotic zone in the ETNP does not share the Fe-NO2 pattern, but instead declines with depth similar to particulate P (Fig. 5). This similarity between particulate Ni and P indicates that the cycling of particulate Ni is primarily controlled by the remineralization of biotic particles. Isotopic evidence also does not support active Ni cycling onto Fe and Mn oxides in the ETNP. Laboratory experiments have shown preferential sorption of light Ni isotopes to Fe and Mn oxides $(\Delta^{60}\text{Ni}_{\text{particulate-aqueous}} = -0.35 \text{ to } -3.4\%)$ (Wasylenki et al., 2015; Gueguen et al., 2018; Sorensen et al., 2020). In natural waters, Vance et al (2016) also found significant removal of light dissolved Ni isotopes across the Black Sea chemocline, with a Δ^{60} Ni_{particulate-aqueous} ~ -4‰, which was attributed to the formation and dissolution of Mn oxides. More recently, preferential remobilization of light dissolved Ni isotopes from marine sediments during early diagenesis has been attributed to cycles of Mn-oxide dissolution and precipitation (Little et al., 2020). In the ETNP, however particulate δ^{60} Ni and Ni/P do not vary synchronously with the particulate Mn and dissolved Mn concentrations (Figs. 2 and 5) in a way which would suggest significant adsorption to Mn oxides. Although Ni sorption onto particles in low oxygen waters through Fe oxyhydroxide formation has been observed in the ETSP ODZ where particulate Fe is one order of magnitude lower than that of the ETNP ODZ (Lee et al., 2018), there is no evidence for the process in this study. The particulate Fe concentrations in the ETNP low oxygen water can be as high as 30 nmol kg⁻¹ (Fig. 5), however, there is no corresponding increase in particulate Ni or Ni/P ratios nor a shift in particulate δ⁶⁰Ni (Fig. 5), which indicates that the presence of Fe oxyhydroxide may not be the determinant factor for Ni sorption. Thus, the particle δ^{60} Ni values observed at all depths in the ETNP can mostly be explained as originating in the euphotic zone from biological uptake into phytoplankton, with three lower particulate δ^{60} Ni samples in the low oxygen water possibly reflecting NiS formation (although if so the influence on the dissolved phase must have been too small to yield significant changes in dissolved δ^{60} Ni).

4.5. Comparison of Pacific and Atlantic dissolved [Ni]– $\delta^{60} Ni$ systematics

Although the study of δ^{60} Ni systematics in the global open oceans is still relatively new, our new data in combination with previously published data appear to show subtle but distinct dissolved [Ni]– δ^{60} Ni patterns between the Atlantic and the Pacific Oceans (Fig. 7A and B; Cameron and Vance, 2014; Takano et al., 2017; Wang et al., 2019; Archer et al., 2020; Yang et al., 2020). Between 3 and 5 nmol kg⁻¹ of dissolved Ni, δ^{60} Ni values in the Atlantic are consistently about 0.1–0.15‰ lighter than the Pacific. While only slightly larger than our analytical uncertainty on dissolved δ^{60} Ni measurements (of ~0.08‰), this subtle basin-scale difference may point to an important control on global Ni cycling.

Further examination of the relationship between [Ni]⁻¹ and δ^{60} Ni in the Pacific and the Atlantic shows two separate and strong linear correlations, which are statistically significantly different from each other (p < 0.001; Supplementary Appendix B). Each relationship is consistent with two-endmember mixing, with the Atlantic and Pacific each having a unique deep-water endmember (Fig. 7C and D). The linear relationships converge at a point where $\delta^{60}Ni$ is at $\pm 1.7\%$ and [Ni] is at 2 nmol kg⁻¹, indicating a common surface ocean endmember. At depth, however, the mixing line in the Atlantic suggests a deep endmember with δ^{60} Ni = +1.31-1.29‰ and [Ni] = 6-7 nmol kg⁻¹(Fig. 7C), whereas the Pacific's mixing line suggests a distinct endmember with δ^{60} Ni + 1.40–1.35‰ and Ni concentrations between 6 and 10 nmol kg⁻¹(Fig. 7D). Data from the deep Indian sector of the Southern Ocean (>1000 m) lies between endmembers from the deep Atlantic and the Pacific with an average of $\pm 1.33 \pm 0.08\%$ (2 σ) (Fig. 7C and D; Wang et al., 2019).

It therefore appears as if dissolved δ^{60} Ni gets progressively heavier with the aging of deep waters, which is unexpected for an element where there is a biological preference for uptake of the lighter isotopes. Comparatively, dissolved δ¹¹⁴Cd in deep waters has a different trend, despite Ni and Cd sharing the same vertical isotopic fractionation trend (i.e. the preferential biological uptake of light isotopes) and both metals being isotopically lighter in deep-sea settling biogenic particles than the ambient seawater (Janssen et al., 2019; Takano et al., 2020). Deepwater dissolved δ¹¹⁴Cd remains consistent or decreases by a subtle amount from the Southern Ocean ($\pm 1.21 \pm 0.36\%$, 2σ) to the Pacific ($\pm 1.14 \pm 0.37\%$, 2σ) which is thought to be a result of the remineralization of sinking isotopically light particles (Janssen et al., 2017). Since the remineralization of particulate matter should similarly supply light Ni to deep waters, the increase in δ^{60} Ni with water age suggests that there are other heavy Ni sources in the deep ocean.

Based on a recent study of two suboxic sediment cores sampled in the East Pacific Rise, this source of isotopically heavy Ni into the deep Pacific could result from processes during the early diagenesis of marine sediments (Little et al., 2020). Prior to the study of Little et al. (2020), analyses of oceanic Ni budget showed significant flux and isotopic mass imbalances (Vance et al., 2016; Ciscato et al., 2018). Major inputs of Ni (riverine dissolved Ni and Ni from mineral dust) are enriched with light Ni isotopes (average of δ^{60} Ni = +0.79‰) compared to the ocean inventory, and have an estimated flux of 3.7×10^8 mol/yr. By contrast, the estimated output flux, which is mainly based on data collected from oxic sediments, ranges from 7.2 to 17×10^8 mol/yr with δ^{60} Ni = +1.5% (Ciscato et al., 2018). If the cycling of Ni isotopes is at steady state, the imbalance must be resolved by either adding a new heavy Ni input, or by correcting the output flux and isotopic composition both of which might have been overestimated (Cameron and Vance, 2014; Vance et al., 2016; Ciscato et al., 2018). Therefore, the discovery of diagenetic remobilization of isotopically heavy Ni (at $\sim +3\%$) may be the missing mechanism that balances the marine Ni budget (Little et al., 2020; Gueguen and Rouxel, 2021). Given the

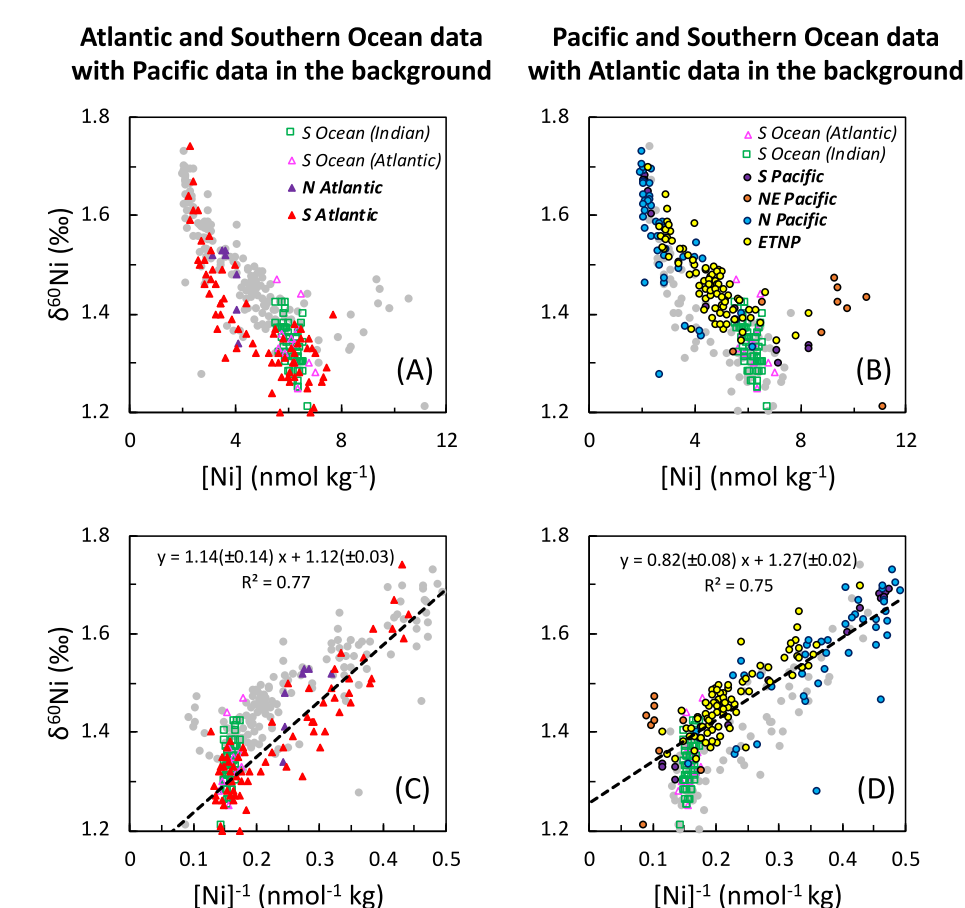


Fig. 7. Global patterns of dissolved Ni concentrations and Ni isotope compositions throughout the world ocean (Cameron and Vance, 2014; Takano et al., 2017; Wang et al., 2019; Archer et al., 2020; Yang et al., 2020; this study). Plots include previously published data and highlight data from the Atlantic Ocean and Southern Ocean with Pacific Ocean data as gray points (A and C), or highlight data from the Pacific and Southern Ocean, with Atlantic data shown in gray (B and D). Dashed lines are linear regressions between δ^{60} Ni and [Ni]⁻¹ for Atlantic and Pacific Ocean data (Southern Ocean data is not used). Errors in the regression equations denote 2σ . The Pacific and Atlantic regressions are significantly different from each other (p < 0.001; see supplementary file).

ubiquitous nature of Ni inputs from suboxic sediments, Little et al., calculated that this flux indeed does balance overall Ni inputs and outputs in the ocean. This flux of isotopically heavy Ni from sediments could also explain why the relatively older Pacific deep waters are isotopically heavier than deep waters in the Atlantic.

Here, based on the $\sim 0.1\%e$ δ^{60} Ni difference between the deep Pacific and Atlantic pools, we estimate that 0.36-0.57 nmol kg $^{-1}$ of the 6-10 nmol kg $^{-1}$ Ni in the Pacific deep Ni pool can be attributed to this benthic Ni source. Thus, we would calculate benthic inputs of $1.8-2.9 \times 10^8$ mol/yr given a global deep ocean volume (>1000 m) of $\sim 1 \times 10^{21}$ kg and a deep-water turnover time of ~ 1000 yrs, which is comparable with the estimation by Little et al. (2020). This use of interbasin comparison of dissolved δ^{60} Ni to calculate fluxes may hint at a new use of δ^{60} Ni for understanding biogeochemical processes on the past earth. While the marine sediment δ^{114} Cd record seems to reflect productivity over geological time periods (e.g.

Georgiev et al., 2015; John et al., 2017; Zhang et al., 2018), the δ^{60} Ni record may be a proxy for fluxes of diagenetically released materials, since there seems to be an association between deep water δ^{60} Ni and early diagenesis. The reconstruction of coupled δ^{114} Cd– δ^{60} Ni in paleo-deep water may therefore provide insight into the interactions between the biological pump and early diagenesis.

5. CONCLUSION

In this study we have presented data on elemental cycling within the ETNP ODZ with a focus on Ni and Ni stable isotopes. Although biological uptake of light Ni must be invoked to explain why different water masses have different [Ni]- δ^{60} Ni characteristics, we note that endmember mixing between AAIW, NEPIW, 13CW and ESW can explain the majority of our dataset. Further, consistent with previous studies, a biological uptake of light Ni can be explained either through simple Rayleigh fractionation, or

through Rayleigh fractionation where there are separate bioavailable and non-bioavailable Ni pools. We note that analyses of particulate δ^{60} Ni in regions where Ni is more depleted may help to distinguish these two possibilities. Lastly, our data does not provide any evidence for unique Ni cycling processes in the ODZ such as sulfide precipitation or Ni sorption/desorption through Fe/Mn redox chemistry, as has been observed in the other ODZs and the Black Sea.

Globally, in combination with other datasets, we find basin-scale differences between the [Ni]– δ^{60} Ni systematics in the Pacific and Atlantic. In the Pacific we find two major endmembers with lower δ^{60} Ni at the surface (+1.7‰) compared to at depth (~+1.4‰). While the Atlantic has a similar shallow Ni endmember, the inferred deep-sea endmember is 0.1‰ lighter than in the Pacific (~+1.3‰). Two sediment cores from the East Pacific Rise suggest that heavier Ni isotopes are preferentially released during early diagenesis, presumably due to adsorption of lighter Ni onto Mn oxides (Little et al., 2020). Further studies may help to clarify whether this process is ubiquitous, and whether it is the cause for the different deep-ocean δ^{60} Ni endmembers discussed here.

Declaration of Competing Interest

The authors declare that they have no known competing financial interests or personal relationships that could have appeared to influence the work reported in this paper.

ACKNOWLEDGEMENT

We would like to thank Irit Tal (USC), Wen-Hsuan Liao (Academia Sinica), Ethan Goddard (USF) for technical support. We acknowledge the Captains and Crew of the R/V Revelle and R/V Sikuliaq for sampling support. We thank Associated Editor Susan Little for handling this paper, and Dr. Bleuenn Guéguen and two anonymous reviewers for providing insightful comments. This work was supported by the National Science Foundation (NSF-OCE #1736896 to S.G.J. and T.M.C., #1636332 to S.G.J. and J. W.M., and #1737136 to T.M.C.), the Ministry of Science and Technology, Taiwan (MOST 109-2116-M-001-019 to K.F.H.), and the Taiwan-USC Postdoctoral Fellowship Program (S.C.Y).

APPENDIX A. SUPPLEMENTARY MATERIAL

Supplementary data to this article can be found online at https://doi.org/10.1016/j.gca.2021.07.004.

REFERENCES

- Almazan-Becerril A. (2008) Maximum efficiency of charge. Separation of photosystem II of the phytoplankton community in the Eastern Tropical North Pacific off Mexico: a nutrient stress diagnostic tool? *Cienc. Mar.* **34**(1), 29–43.
- Archer C., Vance D., Milne A. and Lohan M. C. (2020) The oceanic biogeochemistry of nickel and its isotopes: new data from the South Atlantic and the Southern Ocean biogeochemical divide. *Earth Planet. Sci. Lett.* 535, 116–118.
- Bianchi D., Weber T. S., Kiko R. and Deutsch C. (2018) Global niche of marine anaerobic metabolisms expanded by particle microenvironments. *Nat. Geosci.* 11(4), 263–268.

- Boiteau R. M., Till C. P., Ruacho A., Bundy R. M., Hawco N. J., McKenna A. M., Barbeau K. A., Bruland K. W., Saito M. A. and Repeta D. J. (2016) Structural characterization of natural nickel and copper binding ligands along the US GEOTRACES Eastern Pacific Zonal Transect. Front. Mar. Sci. 3, 243.
- Bostock H. C., Opdyke B. N. and Williams M. J. M. (2010) Characterising the intermediate depth waters of the Pacific Ocean using δ^{13} C and other geochemical tracers. *Deep Sea Res. Part I* **57**(7), 847–859.
- Boyle E. A., Huested S. S. and Jones S. P. (1981) On the distribution of copper, nickel, and cadmium in the surface waters of the North Atlantic and North Pacific Ocean. *J. Geophys. Res. Oceans* **86**(C9), 8048. doi.10.1029/JC086iC09p08048.
- Bruland K. W. (1980) Oceanographic distributions of cadmium, zinc, nickel, and copper in the North Pacific. *Earth Planet. Sci. Lett.* 47(2), 176–198.
- Cameron V., Vance D., Archer C. and House C. H. (2009) A biomarker based on the stable isotopes of nickel. *Proc. Natl.* Acad. Sci. U.S.A. 106(27), 10944–10948.
- Cameron V. and Vance D. (2014) Heavy nickel isotope compositions in rivers and the oceans. *Geochim. Cosmochim. Acta* 128, 195–211.
- Ciscato E. R., Bontognali T. R. R. and Vance D. (2018) Nickel and its isotopes in organic-rich sediments: implications for oceanic budgets and a potential record of ancient seawater. *Earth Planet. Sci. Lett.* 494, 239–250.
- Conway T. M. and John S. G. (2015) Biogeochemical cycling of cadmium isotopes along a high-resolution section through the North Atlantic Ocean. *Geochim. Cosmochim. Acta* 148, 269– 283.
- Conway T. M., Rosenberg A. D., Adkins J. F. and John S. G. (2013) A new method for precise determination of iron, zinc and cadmium stable isotope ratios in seawater by double-spike mass spectrometry. *Anal. Chim. Acta* **793**, 44–52.
- Conway T. M., Horner T. J., Plancherel Y. and González A. G. (2021) A decade of progress in understanding cycles of trace elements and their isotopes in the ocean. *Chem. Geol.* 580, 120381.
- Cullen J. T. and Sherrell R. M. (1999) Techniques for determination of trace metals in small samples of size-fractionated particulate matter: phytoplankton metals off central California. *Mar. Chem.* 67(3-4), 233–247.
- Cutter G. A., Casciotti K., Croot P., Geibert W., Heimbürger L. E., Lohan M. C., Planquette H., and van de Flierdt T. (2017) Sampling and sample-handling protocols for GEOTRACES cruises. Version 3, August 2017. Toulouse, France, GEOTRACES International Project Office, 139pp. & Appendices.
- Dupont C. L., Barbeau K. and Palenik B. (2008) Ni uptake and limitation in marine Synechococcus strains. Appl. Environ. Microbiol. 74, 23–31.
- Dupont C. L., Buck K. N., Palenik B. and Barbeau K. (2010) Nickel utilization in phytoplankton assemblages from contrasting oceanic regimes. *Deep Sea Res. Part I* 57, 553–566.
- Dupont C. L., Johnson D. A., Phillippy K., Paulsen I. T., Brahamsha B. and Palenik B. (2012) Genetic identification of a high-affinity Ni transporter and the transcriptional response to Ni deprivation in *Synechococcus* sp. strain WH8102. *Appl. Environ. Microbiol.* 78, 7822–7832.
- Elliott T. and Steele R. C. J. (2017) The isotope geochemistry of Ni. *Rev. Mineral. Geochem.* **82**(1), 511–542.
- Evans N., Boles E., Kwiecinski J. V., Mullen S., Wolf M., Devol A.
 H., Moriyasu R., Nam S., Babbin A. R. and Moffett J. W.
 (2020) The role of water masses in shaping the distribution of redox active compounds in the Eastern Tropical North Pacific oxygen deficient zone and influencing low oxygen concentra-

- tions in the eastern Pacific Ocean. Limnol. Oceanogr. 65(8), 1688-1705
- Fiedler P. C. and Talley L. D. (2006) Hydrography of the eastern tropical Pacific: a. review. *Prog. Oceanogr.* **69**(2-4), 143–180.
- Glass J. B., Kretz C. B., Ganesh S., Ranjan P., Seston S. L., Buck K. N., Landing W. M., Morton P. L., Moffett J. W., Giovannoni S. J., Vergin K. L. and Stewart F. J. (2015) Meta-omic signatures of microbial metal and nitrogen cycling in marine oxygen minimum zones. Front. Microbiol. 6, 998.
- Georgiev S. V., Horner T. J., Stein H. J., Hannah J. L., Bingen B. and Rehkämper M. (2015) Cadmium-isotopic evidence for increasing primary productivity during the Late Permian anoxic event. *Earth Planet. Sci. Lett.* 410, 84–96.
- Gueguen B. and Rouxel O. (2021) The Nickel isotope composition of the authigenic sink and the diagenetic flux in modern oceans. *Chem. Geol.* **563** 120050.
- Gueguen B., Sorensen J. V., Lalonde S. V., Peña J., Toner B. M. and Rouxel O. (2018) Variable Ni isotope fractionation between Fe-oxyhydroxides and implications for the use of Ni isotopes as geochemical tracers. *Chem. Geol.* **481**, 38–52.
- Guinoiseau D., Galer S. J. G., Abouchami W., Frank M., Achterberg E. P. and Haug G. H. (2019) Importance of cadmium sulfides for biogeochemical cycling of Cd and its isotopes in Oxygen Deficient Zones-A case study of the Angola Basin. Glob. Biogeochem. Cycles 33(12), 1746–1763.
- Hawco N. J., Yang S.-C., Foreman R. K., Funkey C. P., Dugenne M., White A. E., Wilson S. T., Kelly R. L., Bian X., Huang K.-F., Karl D. M. and John S. G. (2020) Metal isotope signatures from lava-seawater interaction during the 2018 eruption of Kīlauea. *Geochim. Cosmochim. Acta* 282, 340–356.
- Heller M. I., Lam P. J., Moffett J. W., Till C. P., Lee J.-M., Toner B. M. and Marcus M. A. (2017) Accumulation of Fe oxyhydroxides in the Peruvian oxygen deficient zone implies nonoxygen dependent Fe oxidation. *Geochim. Cosmochim. Acta* 211, 174–193.
- Ho T.-Y. (2013) Nickel limitation of nitrogen fixation in *Trichodesmium. Limnol. Oceanogr.* **58**(1), 112–120.
- Ho T.-Y., Pan X., Yang H.-H., Wong G. T. F. and Shiah F.-K. (2015) Controls on temporal and spatial variations of phytoplankton pigment distribution in the Northern South China Sea. *Deep Sea Res. Part II* 117, 65–85.
- Hudson R. J. M. and Morel F. M. M. (1993) Trace metal transport by marine microorganisms: implications of metal coordination kinetics. *Deep Sea Res. Part I* 40(1), 129–150.
- Janssen D. J., Conway T. M., John S. G., Christian J. R., Kramer D. I., Pedersen T. F. and Cullen J. T. (2014) Undocumented water column sink for cadmium in open ocean oxygen-deficient zones. *Proc. Natl. Acad. Sci. U.S.A.* 111(19), 6888–6893.
- Janssen D. J. and Cullen J. T. (2015) Decoupling of zinc and silicic acid in the subarctic northeast Pacific interior. *Mar. Chem.* 177, 124–133.
- Janssen D. J., Abouchami W., Galer S. J. G. and Cullen J. T. (2017) Fine-scale spatial and interannual cadmium isotope variability in the subarctic northeast Pacific. *Earth Planet. Sci. Lett.* 472, 241–252.
- Janssen D. J., Abouchami W., Galer S. J. G., Purdon K. B. and Cullen J. T. (2019) Particulate cadmium stable isotopes in the subarctic northeast Pacific reveal dynamic Cd cycling and a new isotopically light Cd sink. *Earth Planet. Sci. Lett.* 515, 67–78.
- John S. G., Kunzmann M., Townsend E. J. and Rosenberg A. D. (2017) Zinc and cadmium stable isotopes in the geological record: a case study from the post-snowball Earth Nuccaleena cap dolostone. *Palaeogeogr. Palaeoclimatol. Palaeoecol.* 466, 202–208.
- Lam P. and Kuypers M. M. M. (2011) Microbial nitrogen cycling processes in oxygen minimum zones. *Annu. Rev. Mar. Sci.* 3(1), 317–345.

- Lee J.-M., Heller M. I. and Lam P. J. (2018) Size distribution of particulate trace elements in the US GEOTRACES Eastern Pacific Zonal Transect (GP16). Mar. Chem. 201, 108–123.
- Little S. H., Archer C., McManus J., Najorka J., Wegorzewski A. V. and Vance D. (2020) Towards balancing the oceanic Ni budget. *Earth Planet. Sci. Lett.* 547, 116461. doi:10.1016/j.epsl.2020.116461.
- Mackey D. J., O'Sullivan J. E., Watson R. J. and Dal Pont G. (2002) Trace metals in the Western Pacific: temporal and spatial variability in the concentrations of Cd, Cu, Mn and Ni. *Deep Sea Res. Part I* 49(12), 2241–2259.
- Middag R., de Baar H. J., Bruland K. W. and van Heuven S. M. (2020) The distribution of nickel in the west-Atlantic Ocean, its relationship with phosphate and a comparison to cadmium and zinc. Front. Mar. Sci. 7, 105.
- Moffett J. W. (2020). Iron, manganese and nutrient data from four cruises in the eastern tropical North Pacific, 2012 to 2018. Biological and Chemical Oceanography Data Management Office (BCO-DMO). (Version 1) Version Date 2020-11-02, doi:10.26008/1912/bco-dmo.828183.1.
- Moffett J., Goepfert T. and Naqvi S. (2007) Reduced iron associated with secondary nitrite maxima in the Arabian Sea. *Deep Sea Res. Part I* **54**, 1341–1349.
- Moriyasu R., Evans N., Bolster K. M., Hardisty D. S. and Moffett J. W. (2020) The distribution and redox speciation of iodine in the Eastern Tropical North Pacific Ocean. *Glob. Biogeochem. Cycles* 34 e2019GB006302.
- Ohnemus D. C., Rauschenberg S., Cutter G. A., Fitzsimmons J. N., Sherrell R. M. and Twining B. S. (2017) Elevated trace metal content of prokaryotic communities associated with marine oxygen deficient zones. *Limnol. Oceanogr.* **62**, 3–25.
- Peacock C. L. and Sherman D. M. (2007) Sorption of Ni by birnessite: Equilibrium controls on Ni in seawater. *Chem. Geol.* **238**(1-2), 94–106.
- Price N. M. and Morel F. M. M. (1991) Colimitation of phytoplankton growth by nickel and nitrogen. *Limnol. Oceanogr.* **36**(6), 1071–1077.
- Ragsdale S. W. (2009) Nickel-based enzyme systems. *J. Biol. Chem.* **284**(28), 18571–18575.
- Rodriguez I. B. and Ho T. Y. (2014) Diel nitrogen fixation pattern of *Trichodesmium*: the interactive control of light and Ni. Sci. Rep. 4, 4445.
- Sclater F. R., Boyle E. and Edmond J. M. (1976) On the marine geochemistry of nickel. *Earth Planet. Sci. Lett.* 31(1), 119–128.
- Siebert C., Nägler T. F. and Kramers J. D. (2001) Determination of molybdenum isotope fractionation by double-spike multicollector inductively coupled plasma mass spectrometry. *Geochem. Geophys. Geosyst.* 2, 2000GC000124.
- Sorensen J. V., Gueguen B., Stewart B. D., Peña J., Rouxel O. and Toner B. M. (2020) Large nickel isotope fractionation caused by surface complexation reactions with hexagonal birnessite. *Chem. Geol.* 537 119481.
- Takano S., Tanimizu M., Hirata T., Shin K.-C., Fukami Y., Suzuki K. and Sohrin Y. (2017) A simple and rapid method for isotopic analysis of nickel, copper, and zinc in seawater using chelating extraction and anion exchange. *Anal. Chim. Acta* 967, 1–11.
- Takano S., Liao W.-H., Tian H.-A., Huang K.-F., Ho T.-Y. and Sohrin Y. (2020) Sources of particulate Ni and Cu in the water column of the northern South China Sea: Evidence from elemental and isotope ratios in aerosols and sinking particles. *Mar. Chem.* 219, 103751. doi:10.1016/ j.marchem.2020.103751.
- Twining B. S., Baines S. B., Vogt S. and Nelson D. M. (2012) Role of diatoms in nickel biogeochemistry in the ocean. *Glob. Biogeochem. Cycles* **26**, GB4001.

- Twining B. S., Nodder S. D., King A. L., Hutchins D. A., LeCleir G. R., DeBruyn J. M., Maas E. W., Vogt S., Wilhelm S. W. and Boyd P. W. (2014) Differential remineralization of major and trace elements in sinking diatoms. *Limnol. Oceanogr.* 59(3), 689–704.
- Vance D., Little S. H., Archer C., Cameron V., Andersen M. B., Rijkenberg M. J. A. and Lyons T. W. (2016) The oceanic budgets of nickel and zinc isotopes: the importance of sulfidic environments as illustrated by the Black Sea. *Philos. Trans. R.* Soc. A 374(2081), 20150294. doi.10.1098/rsta.2015.0294.
- Wang R.-M., Archer C., Bowie A. R. and Vance D. (2019) Zinc and nickel isotopes in seawater from the Indian Sector of the Southern Ocean: the impact of natural iron fertilization versus Southern Ocean hydrography and biogeochemistry. *Chem. Geol.* 511, 452–464.
- Wasylenki L. E., Howe H. D., Spivak-Birndorf L. J. and Bish D. L. (2015) Ni isotope fractionation during sorption to ferrihydrite: implications for Ni in banded iron formations. *Chem. Geol.* 400, 56–64.

- Wedepohl K. H. (2000) The composition of the upper earth's crust and the natural cycles of selected metals. Metals in raw materials. Natural resources. In *Metals and their Compounds in the Environment, Part 1* (ed. E. Merian). John Wiley and Sons, New York, pp. 3–16.
- Yang S. C., Hawco N. J., Gonzalez P. P., Bian X., Huang K. F., Zhang R. and John S. G. (2020) A new purification method for Ni and Cu stable isotopes in seawater provides evidence for widespread Ni isotope fractionation by phytoplankton in the North Pacific. *Chem. Geol.* 547 119662.
- Zhang Y., Wen H., Zhu C., Fan H. and Cloquet C. (2018) Cadmium isotopic. Evidence for the evolution of marine primary productivity and the biological extinction event during the Permian-Triassic crisis from the Meishan section, South China. *Chem. Geol.* **481**, 110–118.

Associate editor: Susan Halsall Little